International Journal of Minerals, Metallurgy and Materials
Volume 26, Number 10, October 2019, Page 1274
https://doi.org/10.1007/s12613-019-1860-3

Microstructure, mechanical, and corrosion properties of extruded low-alloyed Mg–*x*Zn–0.2Ca alloys

Ying-zhong Ma[1)], *Chang-lin Yang*[2)], *Yun-jin Liu*[1)], *Fu-song Yuan*[3)], *Shan-shan Liang*[4)], *Hong-xiang Li*[1)], *and Ji-shan Zhang*[1)]

1) State Key Laboratory for Advanced Metals and Materials, University of Science and Technology Beijing, Beijing100083, China
2) State Key Laboratory of Solidification Processing, Northwestern Polytechnical University, Xi'an 710072, China
3) Center of Digital Dentistry, Peking University School and Hospital of Stomatology, Beijing 100081, China
4) Second Clinical Division, Peking University Hospital of Stomatology, Beijing 100081, China
(Received: 30 October 2018; revised: 27 May 2019; accepted: 3 June 2019)

Abstract: The microstructure, mechanical, and corrosion properties of extruded low-alloyed Mg–*x*Zn–0.2Ca (x = 0, 1.0, 2.0, 3.0) alloys were investigated in this study. Findings from scanning electron microscope, X-ray diffraction and transmission electron microscopy results indicate that the amount of ternary $Ca_2Mg_6Zn_3$ phase, as the only secondary phase in 1.0Zn, 2.0Zn, and 3.0Zn alloys, gradually increases with the addition of Zn, while the Mg_2Ca phase was observed in the Mg–0.2Ca alloy only. Zn has a strong effect on the orientation and intensity of textures, which also influence mechanical behaviors, as revealed by electron back-scatter diffraction. Among all the alloys, the Mg–2.0Zn–0.2Ca alloy obtains the maximum tensile strength (278 MPa) and yield strength (230 MPa). Moreover, Zn addition has an evident influence on the corrosion properties of Mg–*x*Zn–0.2Ca alloy, and Mg–1.0Zn–0.2Ca alloy exhibits the minimum corrosion rate. This paper provides a novel low-alloyed magnesium alloy as a potential biodegradable material.

Keywords: magnesium alloy; Mg–Zn–Ca alloy; extrusion; microstructure; mechanical properties; corrosion properties; textures

1. Introduction

Magnesium and its alloys have attracted great attention in recent years due to their excellent mechanical properties and biodegradability. Magnesium and its alloys have low density and elastic modulus close to that of natural bone, therefore ensuring the reduction or elimination of the stress shielding effect [1] caused by the substantial mismatch in the elastic modulus between natural bone and implant metals. However, the wide application of magnesium alloys is still limited due to poor corrosion resistance and low strength [2]. Many efforts can be made to improve the strength and corrosion resistance. One effective way to elevate the strength is the conventional thermomechanical processing, which includes extrusion, rolling, and forging, and can eliminate casting defects, induce dynamic recrystallization, and obtain refined grain sizes [3]. The Hall-Petch formula indicates that this process could considerably improve mechanical properties [4]. Another method is the addition of alloying elements, such as rare earth (RE) elements, Al, Zn, and Ca. Zn is one of the most commonly used alloying elements for Mg alloys. The solubility of Zn in Mg is about 1.4wt% at room temperature. A certain amount of Zn can significantly improve the yield strength (YS), ultimate tensile strength (UTS), and elongation of magnesium alloys. Ca, as an essential trace element for the human body, is a candidate that is often added to Mg alloys to replace RE elements. The addition of Zn and Ca to Mg alloys can induce the precipitation of intermetallic compound $Ca_2Mg_6Zn_3$ [4], which contributes to second-phase strengthening and improves the YS and the tensile strength [5]. According to recent studies, Zn content of up to 4wt% in Mg alloy has a peak of UTS and YS that is similar to that achieved with the addition of Ca up to 0.2wt% [6]. With the addition of Ca content up to 0.7wt%,

Corresponding authors: Hong-xiang Li E-mail: hxli@skl.ustb.edu.cn; Ji-shan Zhang E-mail: zhangjs@skl.ustb.edu.cn

the mechanical properties of ZM21 magnesium alloys reach the optimal value related to the refined grain size and the formation of the second phase [7]. Although the mechanical properties can be improved by the alloying of Zn and Ca elements, increased addition of Ca is harmful to corrosion resistance considering the acceleration of micro-galvanic corrosion [8]. In addition, a certain amount of Zn (up to 1.25wt%) can decrease the corrosion rate, but further addition of Zn up to 4wt% can increase the corrosion rate [1]. Thus, the composition should be adjusted to reduce the content of alloying elements if a balance between strength and corrosion resistance needs to be achieved.

Low-alloyed extruded Mg–Zn–Ca alloys have an excellent advantage in obtaining balanced properties. Zhang *et al.* [9] investigated the microstructure and mechanical properties of extruded Mg–1.0Zn–0.5Ca alloy. The alloy extruded at 370°C exhibits elongation of 44% allied with UTS of 215 MPa. The superior properties were attributed to grain refinement and the unique extruded texture. Hofstetter *et al.* [10] investigated the effect of different thermomechanical processing routes on the microstructure and mechanical properties of low-alloyed Mg–1.0Zn–0.3Ca and Mg–0.5Zn–0.15Ca alloys. Studies on extruded low-alloyed Mg–Zn–Ca alloys are still scarce, and current investigations on the extruded Mg–Zn–Ca alloys mainly focus on high-alloyed Mg alloys [3–4,11].

On the basis of the current status of low-alloyed Mg–Zn–Ca alloys, a group of novel low-alloyed Mg–Zn–Ca alloys were prepared in this study by controlling the Zn content. The effect of Zn on the microstructure, mechanical, and corrosion properties of the extruded low-alloyed Mg–Zn–Ca alloys is investigated in particular. Also, the mechanisms on strengthening and variation of corrosion properties in the extruded Mg–Zn–Ca alloys are discussed.

2. Experimental

The Mg–*x*Zn–0.2Ca alloy (x = 0, 1.0, 2.0, 3.0, hereafter denoted as 0Zn, 1.0Zn, 2.0Zn, and 3.0Zn alloys) were prepared from pure Mg ingots (99.99wt%), pure Zn particles (99.99wt%), and Mg–20Ca (with the 20wt% Ca) master alloy heated in a high-purity graphite crucible in an electric resistance furnace under a mixed atmosphere of 1vol% SF_6 and 99vol% CO_2. Then, the crucible was taken out to cool in the air. The ingots were homogenized at 400°C for 12 h before extrusion, and then the ingots that were preheated over 3 hours were extruded into bars (22 mm in diameter) at 325°C and a ram speed of 3 mm/s under an extruded ratio of 30.

To characterize the microstructure, the specimens were prepared by standard metallographic procedures and cut along the extruded direction from the extruded bar. A Carl Zeiss Axio Imager A2m optical microscopy (OM) and a field-emission scanning electron microscope (FE-SEM, Supra 55) equipped with energy dispersive spectrometer (EDS) and electron back-scatter diffraction (EBSD) system were used to observe the microstructure of the specimens. All the specimens were first ground on emery papers to 2000 grit, polished for SEM observation, and then etched by 3vol% nitric acid alcohol solution for OM observation. The EBSD samples were electro-polished in an ACII mixture solution at −20°C under a 20 V applied potential. The average grain size was estimated by a line intercept technique using the OM micrographs. Microstructure examination of the extruded Mg–*x*Zn–0.2Ca alloys was first conducted by X-ray diffraction (XRD) using Rigaku S2 X-ray diffractometer with Cu Kα radiation. Further investigations of second phases were performed by means of transmission electron microscopy (TEM) by using Tecnai G2 F20 (200 kV) microscope equipped with a high-angle annular dark field scanning transmission electron microscopy detector and EDS microanalysis, which can provide a detailed intuitive description of the types, morphology, and distribution of phases. TEM samples were fabricated by using ion thinning technology.

The tensile specimens, with a gage length of 25.0 mm and a diameter of 5.0 mm, were cut from the extruded bar. The tensile direction was parallel to the extruded direction, and an Instron5569 materials testing machine at a displacement rate of 1 mm/min was used. Immersion tests were conducted in simulated body fluid (SBF) using specimens with a dimension of 10 mm × 10 mm × 2 mm, which were ground on emery papers to 2000 grit, cleaned with alcohol, and dried in air. The SBF solution was prepared with deionized water and high-purity chemicals according to the procedure in Ref. [12]. The solution was maintained at a temperature of 37 ± 0.5°C and refreshed every 48 hours throughout the immersion. The samples were removed from the solution after being immersed for 168 h and soaked in chromic acid to remove only corrosion products instead of any amount of Mg base. Subsequently, the specimens were cleaned in absolute ethyl alcohol and in distilled water, then blow-dried with cold wind to observe the surface morphology using SEM.

3. Results

3.1. As-extruded microstructure and textures

Figs. 1 and 2 showing the microstructure of the samples sectioned perpendicular to the extruded direction of

Mg–*x*Zn–0.2Ca alloys obtained by OM and EBSD, respectively. The mean size of the dynamically recrystallized grains is refined from 5.67 to 3.12 μm with an increase in Zn content from 0wt% to 2wt%. However, with further addition of 3wt% Zn, the grain size increased to 4.71 μm again. Second-phase precipitates increased with an increase in Zn content. The secondary phase in 3.0Zn alloy grew larger than that in 0Zn and 1.0Zn, as shown in Fig. 3.

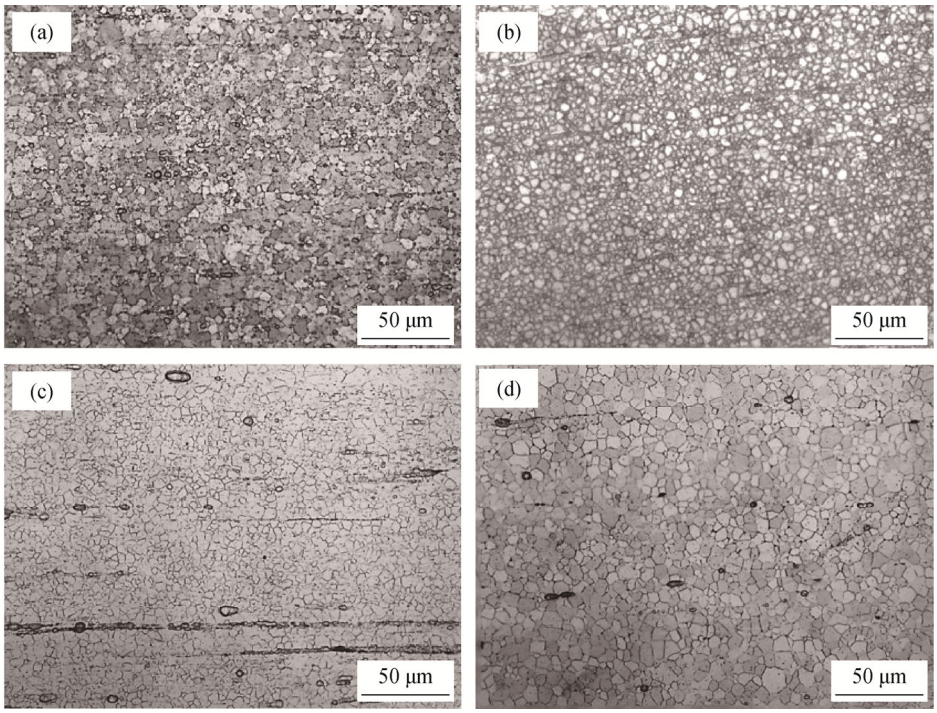

Fig. 1. Microstructure of extruded Mg–*x*Zn–0.2Ca alloys observed by OM perpendicular to the extruded direction: (a) 0Zn; (b) 1.0Zn; (c) 2.0Zn; (d) 3.0Zn.

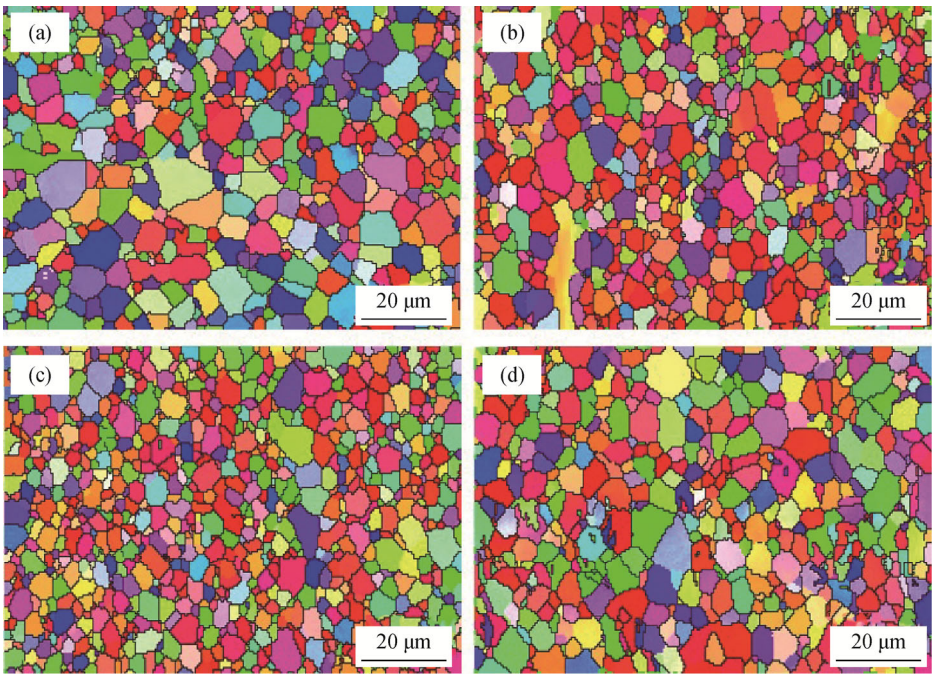

Fig. 2. Microstructure of extruded Mg–*x*Zn–0.2Ca alloys observed by EBSD perpendicular to the extruded direction: (a) 0Zn; (b) 1.0Zn; (c) 2.0Zn; (d) 3.0Zn.

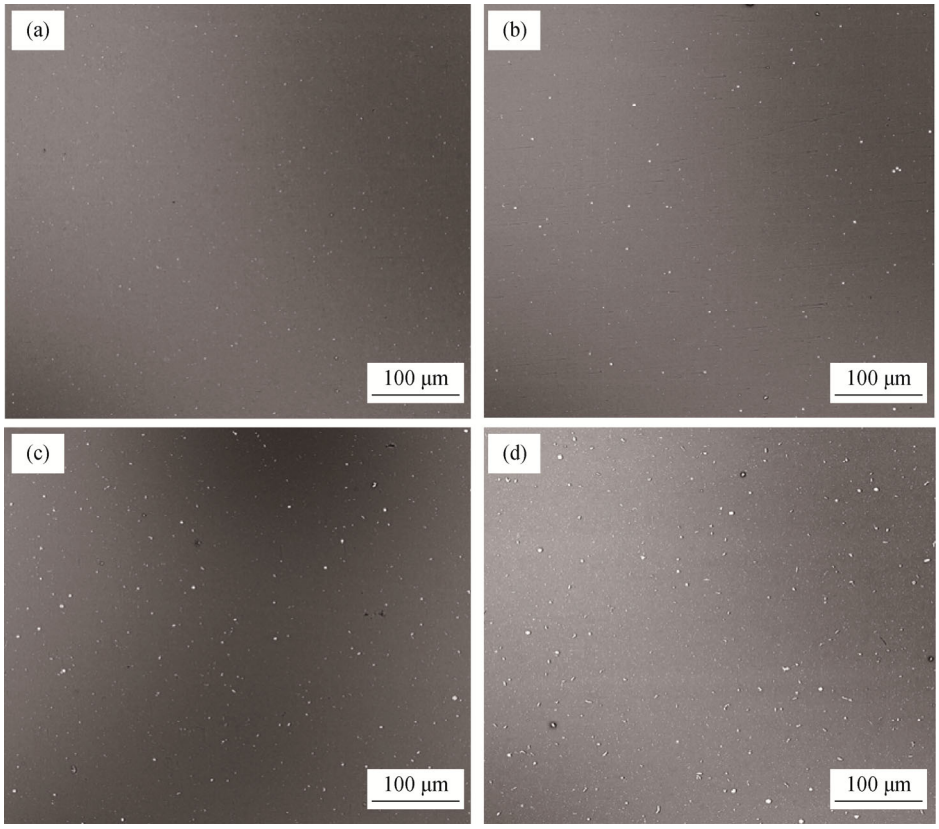

Fig. 3. Microstructure of extruded Mg–*x*Zn–0.2Ca alloys observed by SEM perpendicular to the extruded direction: (a) 0Zn; (b) 1.0Zn; (c) 2.0Zn; (d) 3.0Zn.

The XRD patterns of the extruded alloys are shown in Fig. 4. The alloys mainly consist of α-Mg and $Ca_2Mg_6Zn_3$ ternary phase for the 1.0Zn, 2.0Zn, and 3.0Zn alloys, whereas only α-Mg matrix and a small amount of Mg_2Ca phases are present in the 0Zn alloy. As a result of the low alloying content, characterizing second phases by using XRD patterns only is difficult. The final confirmation of the second phases precipitated in the alloys can be achieved by further TEM analysis.

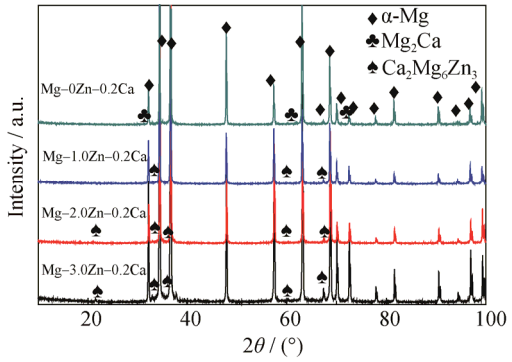

Fig. 4. XRD patterns of the extruded Mg–*x*Zn–0.2Ca specimens.

Fig. 5 exhibits the TEM bright-field images of the extruded 0Zn alloy and corresponding selected area diffraction patterns (SADPs). The alloy matrix is α-Mg solid solution as identified by SADPs, taken along the $[\bar{1}2\bar{1}6]$ zone axis shown in Fig. 5(b). The second phase with triangular granules shown in Fig. 5(a) is Mg_2Ca, identified by SADPs in Fig. 5(c) (zone axis $[01\bar{1}2]$). The EDS results show that the second phase contains 81.8at% Mg and 18.2at% Ca, confirming that the 0Zn alloy consists of α-Mg and Mg_2Ca from both XRD and TEM results.

Fig. 6 demonstrates the TEM bright-field images and corresponding SADPs of the extruded 1.0Zn alloy. The second phase taken along the $[\bar{2}4\bar{2}3]$ zone axis located at the triple junction grain boundary contains 54.2at% Mg, 10.8at% Ca, and 34.9at% Zn, which is speculated to be the ternary $Ca_2Mg_6Zn_3$ phase with a triangular shape and a small size of about 0.5 μm.

Fig. 7 shows the TEM bright-field images and the corresponding SADPs of the extruded 2.0Zn alloy. The 2.0Zn alloys are mainly composed of α-Mg solid solution and the ternary $Ca_2Mg_6Zn_3$ phases, which exhibit different morphologies such as granule, long-stripe, and long-triangle shape containing 49.6at% Mg, 16.2at% Ca, and 34.2at% Zn; 49.2at% Mg, 15.1at% Ca, and 35.7at% Zn; and 52.7at% Mg, 17.4at% Ca, and 29.9at% Zn, respectively. The correspond-

ing calibration results are shown in Fig. 7. In contrast to the 1.0Zn alloy, the ternary $Ca_2Mg_6Zn_3$ phase in the 2.0Zn alloy becomes larger and exhibits various morphologies. In addition, the Mg_2Ca phase observed in the 0Zn alloy is not observed in the 2.0Zn alloy, which is consistent with the XRD pattern shown in Fig. 4.

Fig. 8 shows the TEM bright-field images and corresponding SADPs of the extruded 3.0Zn alloy. Apart from granular and long-stripe shapes, the phase with a rectangular shape can be observed in Fig. 8(c). The phase shown in Fig. 8(a) contains 51.27at% Mg, 15.10at% Ca, and 33.63at% Zn. Combined with SADP analysis, the phases are determined to be $Ca_2Mg_6Zn_3$. The SADPs are not shown here due to similarity to those of the 2.0Zn alloy. Similarly, Mg_2Ca is not found in the TEM bright-field images.

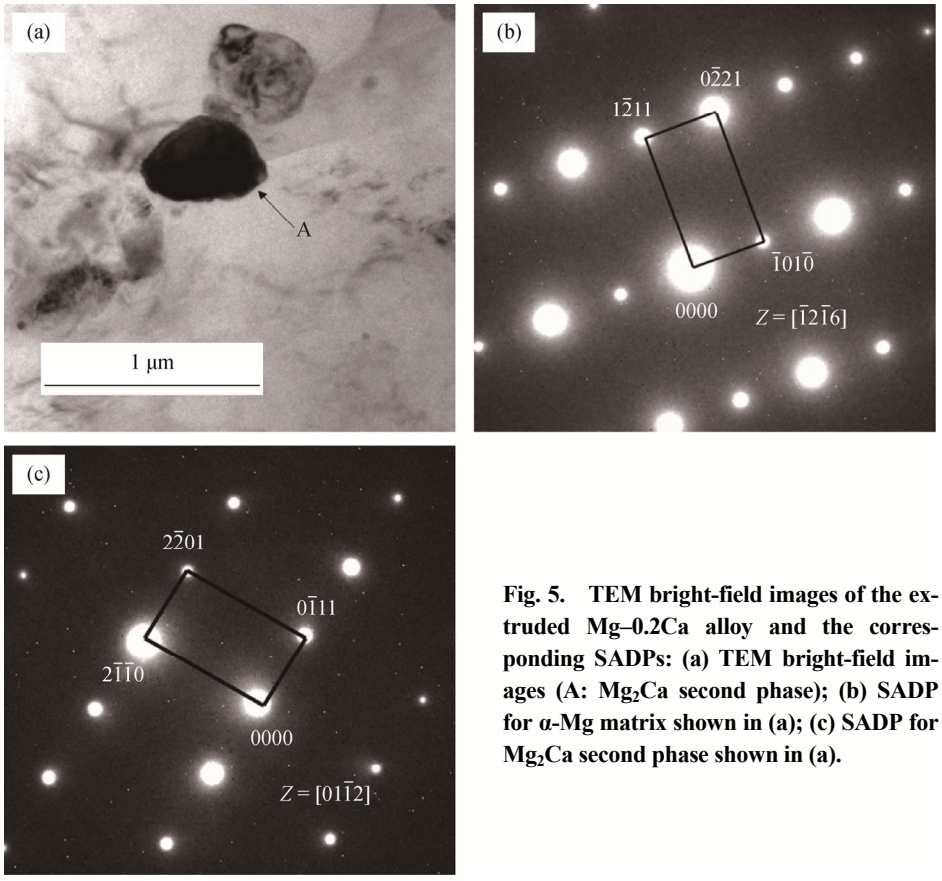

Fig. 5. TEM bright-field images of the extruded Mg–0.2Ca alloy and the corresponding SADPs: (a) TEM bright-field images (A: Mg_2Ca second phase); (b) SADP for α-Mg matrix shown in (a); (c) SADP for Mg_2Ca second phase shown in (a).

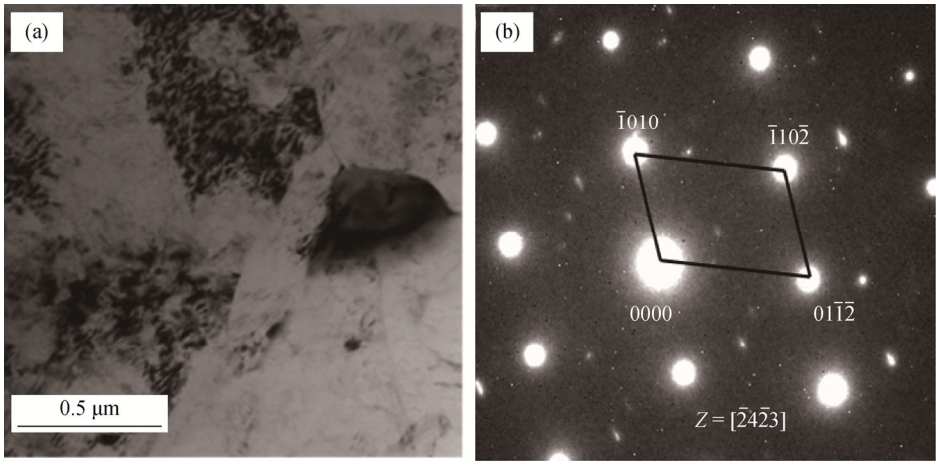

Fig. 6. (a) TEM bright-field images of the extruded Mg–1.0Zn–0.2Ca alloy and (b) the corresponding SADP for second phase shown in (a).

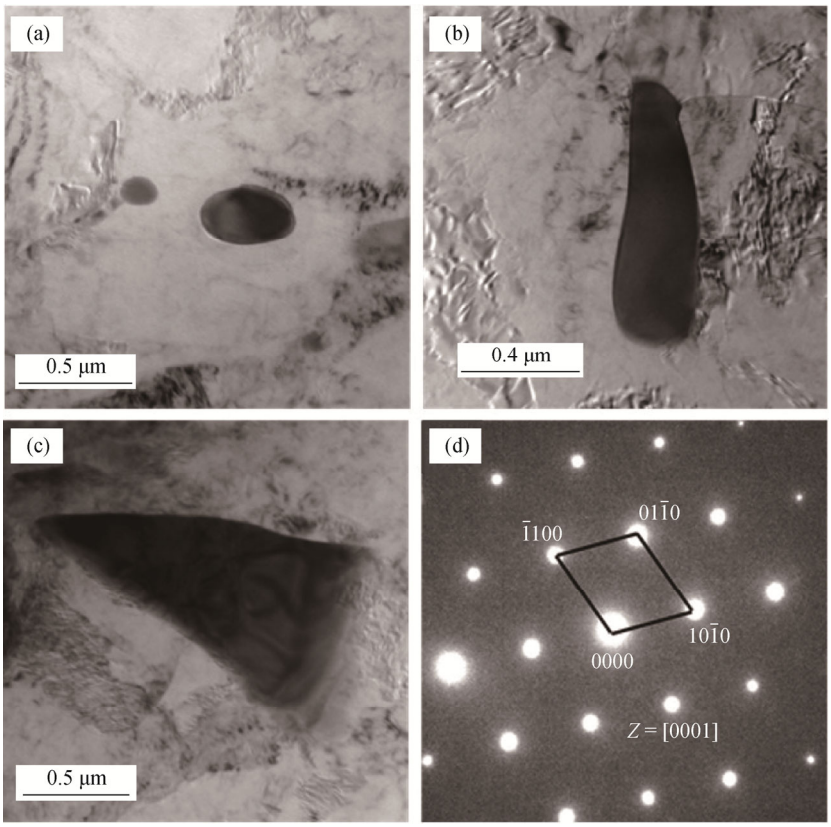

Fig. 7. TEM bright-field images of the extruded Mg–2.0Zn–0.2Ca alloy and the corresponding SADPs: (a–c) TEM bright-field images; (d) SADP for $Ca_2Mg_6Zn_3$ second phase shown in (a).

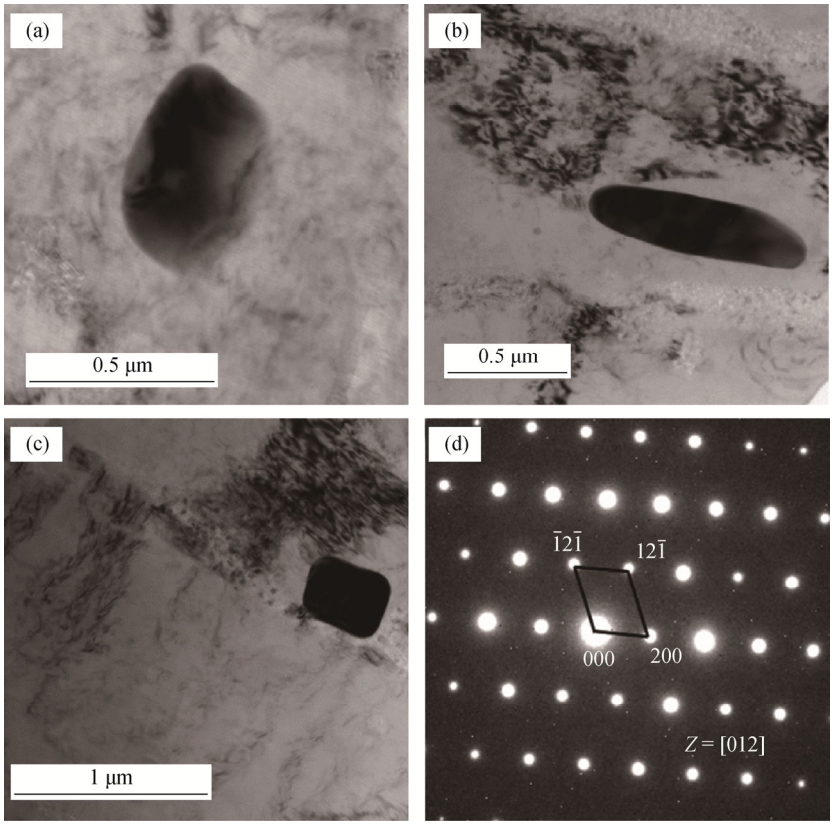

Fig. 8. TEM bright-field images of the extruded Mg–3.0Zn–0.2Ca alloy: (a–c) TEM bright-field images; (d) SADP for $Ca_2Mg_6Zn_3$ second phase shown in (c).

Fig. 9 shows the {0002} pole figures of the extruded alloys, manifesting the effect of textures. The 0Zn alloy has a maximum intensity (6.27) and exhibits basal fiber textures distributed relatively randomly. Then, the poles begin to align parallel to the transverse direction. Three alloys (1.0Zn, 2.0Zn, 3.0Zn) exhibit similar extruded texture and basal poles that have a lower angle distribution away from the transverse direction compared with the 0Zn alloy. This basal fiber texture is the common type found in Mg alloys after extrusion. The basal texture intensity of 1.0Zn decreases to 4.36, which might result from the corresponding dynamically recrystallized process shown in Fig. 2, and is representative of a dispersive texture with the {0002} planet inclining to extruded direction from 0° to 40°. The 2.0Zn alloy exhibits strong basal texture with the highest intensity (6.46) among the four alloys. However, when the Zn content increases to 3wt%, the maximum intensity of textures is weakened from 6.46 to 5.69 with an increase in angle distribution from 25° to 35°.

The fiber textures of four extruded alloys are shown in Fig. 10 in the form of inverse pole figures. The 0Zn alloy exhibits a fiber texture with $[10\bar{1}0]$ orientation parallel to the ED and another relatively strong texture between $[2\bar{1}\bar{1}1]$ and $[2\bar{1}\bar{1}2]$. With the addition of Zn elements, the fiber

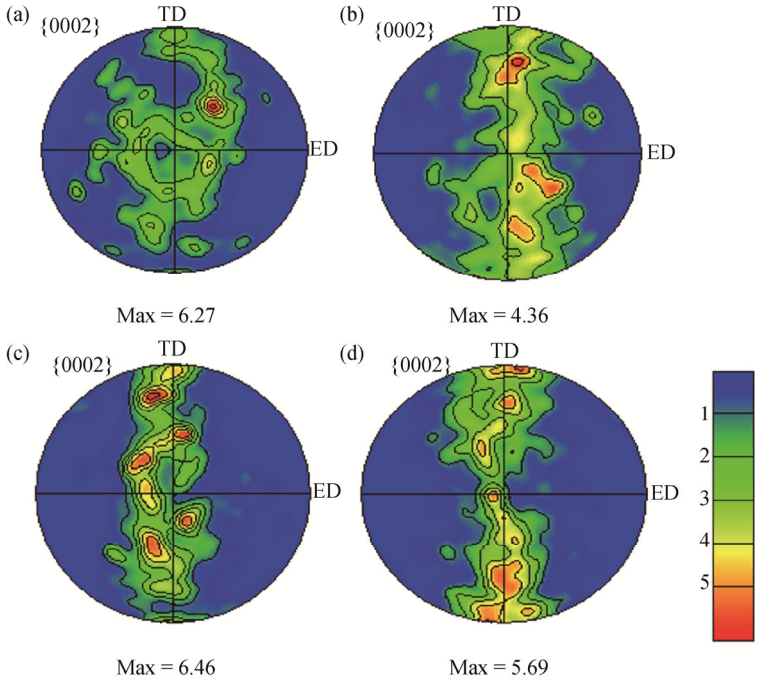

Fig. 9. Pole figure results of Mg–*x*Zn-0.2Ca alloys observed by EBSD: (a) 0Zn; (b) 1.0Zn; (c) 2.0Zn; (d) 3.0Zn.

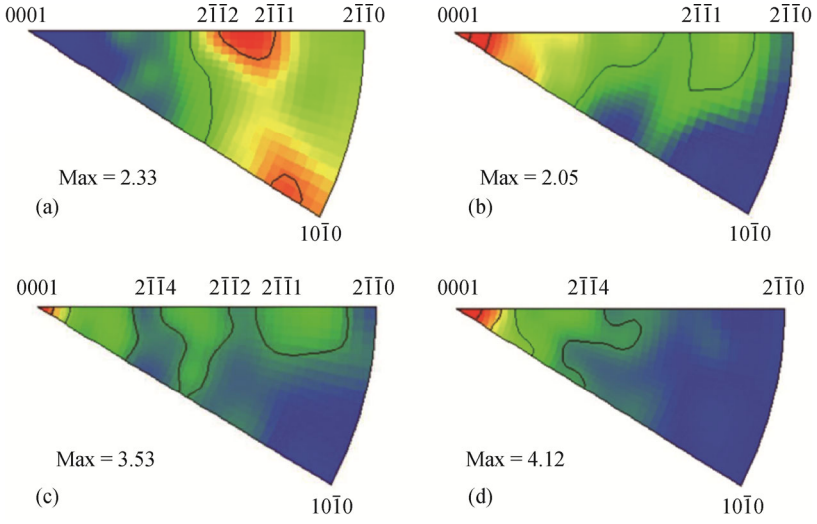

Fig. 10. Inverse pole figure results of Mg–*x*Zn–0.2Ca alloys observed by EBSD: (a) 0Zn; (b) 1.0Zn; (c) 2.0Zn; (d) 3.0Zn.

component is weakened from 2.33 to 2.05 and a typical (0001) fiber texture appears, which was not observed in the 0Zn alloy before. Notably, the Zn element altered the fiber texture orientation visibly. The poles are distributed almost in reverse, as seen from the inverse pole figures, thereby indicating that some crystals are tilted away from the ED. The texture intensities of the alloys increase from 2.05 to 4.12 with the increase in Zn content from 1.0wt% to 3.0wt%, thereby indicating that the addition of Zn contributes to the formation of some strong textures.

3.2. Mechanical and corrosion properties

Fig. 11(a) illustrates the mechanical properties of Mg–*x*Zn–0.2Ca alloys; the corresponding stress–strain curves are given in Fig. 11(b). The YS and the UTS increased obviously with increasing Zn content from 0 to 2wt%. The peak of the YS (230 MPa) and UTS (278 MPa) are obtained for the 2.0Zn alloy, and the YS of the 3.0Zn alloy decreases again. Meanwhile, the elongation decreases from 27.9% to 20.2% for the 0Zn alloy to 2.0Zn alloy and then increases to 21.8% for the 3.0Zn alloy.

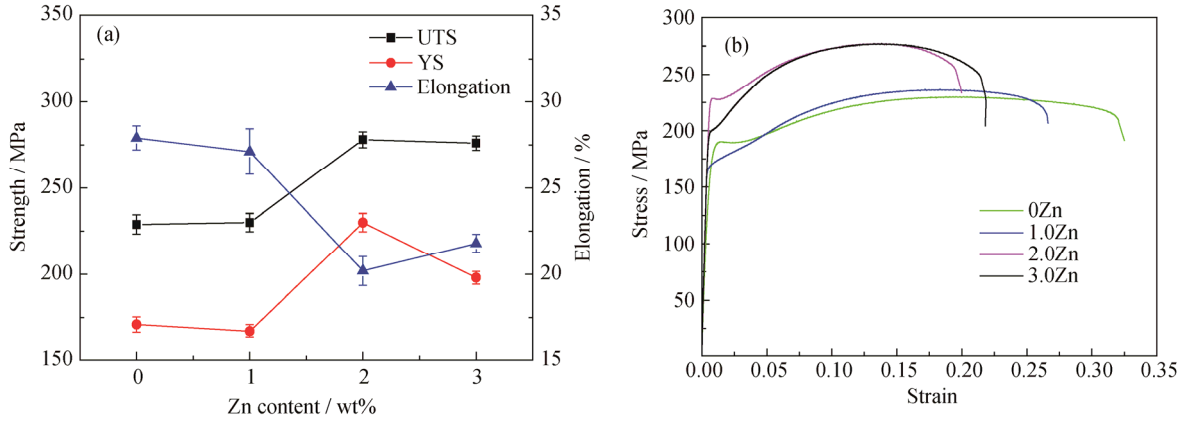

Fig. 11. Mechanical properties (a) and stress–strain curves (b) of the extruded Mg–*x*Zn–0.2Ca alloys.

To evaluate the corrosion properties of Mg–*x*Zn–0.2Ca alloys, corresponding investigations were performed in this study. Fig. 12(a) shows the macrographs without removing the surface corrosion products immersed in SBF solution for 168 h. Serious corrosion behavior occurred in the 2.0Zn alloy and 3.0Zn alloy. In the local areas, corrosion pits even penetrated the entire samples. For the 0Zn alloy, the samples are still intact, being wrapped with a layer of white corrosion products on the surface. The 1.0Zn alloy exhibits a lower corrosion rate than the 0Zn alloy, as evidenced by the fewer white corrosion products on the surface. To quantitatively determine the corrosion resistance of each alloy, the samples were weighed before and after the corrosion products were cleaned. The weight loss of samples immersed in SBF for 168 h was calculated preciously. Fig. 12(b) shows that the weight loss curve first declines and then increases with an increase in Zn content from 0wt% to 3wt%. The minimum weight loss corresponds to 1.0Zn alloy, which is consistent with corrosion morphologies.

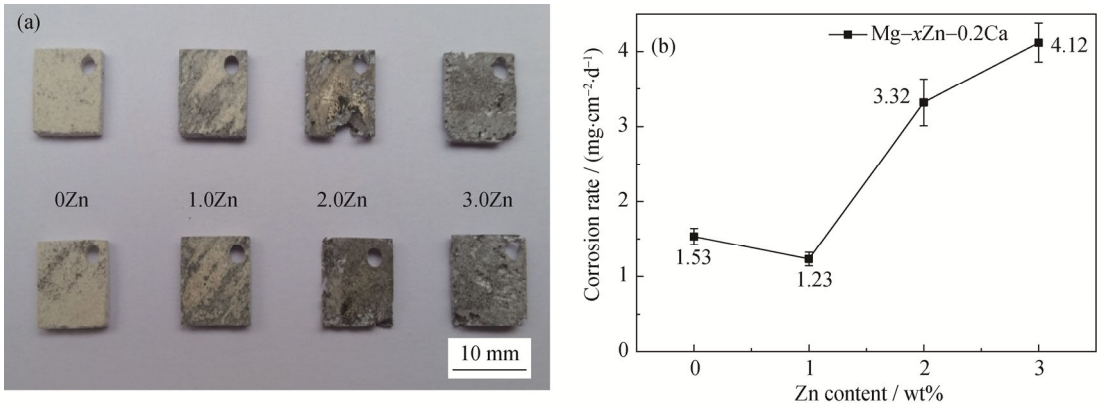

Fig. 12. The surface macrograph without removing the surface corrosion products (a) and the curve of the corrosion rate (b) of Mg–*x*Zn–0.2Ca alloys after being immersed in SBF solution for 168 h at 37°C.

Fig. 13 exhibits the surface morphologies of Mg–*x*Zn–0.2Ca samples after the corrosion products are removed. A mass of corrosion holes is distributed unevenly and a long deep corrosion zone can be observed in some areas of the 0Zn alloy. Compared with the 0Zn alloy, the pitting holes distribute more evenly and shallowly for the 1.0Zn alloy. With an increase in Zn content, the corrosion holes are interconnected and some deeper cavities are even developed throughout the whole sample, especially for the 3.0Zn alloy, which indicates that the corrosion extent is promoted further. The corrosion cavities lead to some parts of exfoliation for the 2.0Zn and 3.0Zn alloys, as seen in Fig. 12(a).

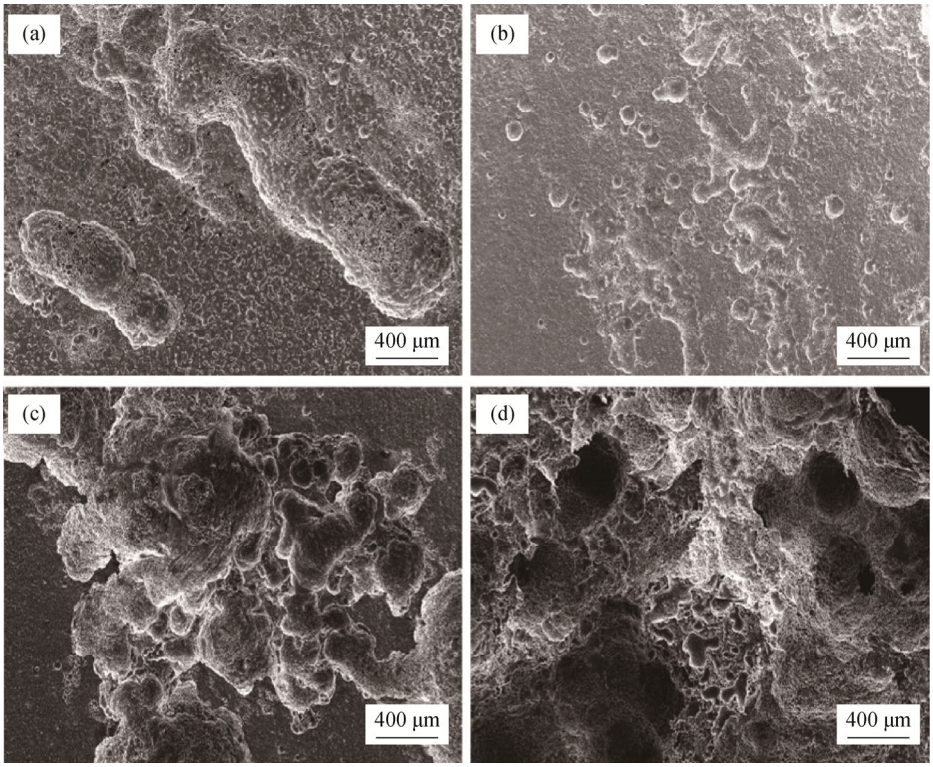

Fig. 13. SEM micrographs of the surface morphology of samples without corrosion products for Mg–*x*Zn–0.2Ca (*x* = 0, 1.0, 2.0, 3.0) alloys: (a) 0Zn; (b) 1.0Zn; (c) 2.0Zn; (d) 3.0Zn.

4. Discussion

The XRD and TEM results shown in Figs. 4–8 indicate that 1.0Zn alloy, 2.0Zn alloy and 3.0Zn alloy are both composed of α-Mg phase and $Ca_2Mg_6Zn_3$ phase except 0Zn alloy is composed of α-Mg phase and Mg_2Ca phase. According to the preceding study [13], the phase composition in the Mg–Zn–Ca alloy mainly depends on the ratio of Zn to Ca. The phase is mainly composed of α-Mg, Mg_2Ca, and $Ca_2Mg_6Zn_3$ phases when the ratio of Zn to Ca is less than 1.2, while it is mainly composed of α-Mg and $Ca_2Mg_6Zn_3$ phase when the ratio of Zn to Ca is more than 1.2 [14]. The ratio of Zn to Ca for 1.0Zn (3.08), 2.0Zn (6.23), and 3.0Zn (9.24) alloys is larger than 1.2, indicating $Ca_2Mg_6Zn_3$ rather than Mg_2Ca can be precipitated in these alloys. Another investigation found that the mixing enthalpy of Mg–Zn (−4 kJ/mol) and Mg–Ca (−6 kJ/mol) is much less than that of Zn–Ca (−22 kJ/mol.) [15], thus indicating that the Ca element reacts more easily with the Zn element than the Mg element. Kubok *et al*. [16] claimed that the ternary $Ca_2Mg_6Zn_3$ coexists with the binary Mg–Zn phase in the as-cast 3.0Zn alloy. In our previous work, however, $Ca_2Mg_6Zn_3$ rather than Mg–Zn intermetallic compounds formed with higher Ca concentration around the α-Mg matrix during the precipitation process; this phenomenon was also reported by other researchers [17–18]. Previous studies reported that the second-phase strengthening effect is the most important reason for the increase of the tensile strength in as-cast alloy [19], and the $Ca_2Mg_6Zn_3$ phase dispersed in the alloy has a strengthening effect [8]. However, the Mg_2Ca phase, which is a brittle phase dispersed along grain boundaries, may easily serve as crack sources, which can propagate and induce brittle fracture, thereby contributing to the decline of tensile strength [8]. Therefore with the addition of Zn element from 0wt% to 2.0wt%, the ternary $Ca_2Mg_6Zn_3$ phase appears and produces a dominant strengthening effect.

Therefore, the 2.0Zn alloy attains the maximum tensile strength. The tensile strength decreases slightly with the further addition of Zn content to 3.0wt% due to the larger mean grain size, which offsets the effect of second-phase precipitation strengthening.

The mechanical properties are also significantly influenced not only by the grain size but also by the textures. The basal slip system played a crucial part in the deformation behavior of magnesium alloys. Texture transformation has a strong effect with the addition of Zn from 0wt% to 1.0wt%, as shown in Figs. 9–10. This finding confirms the existence of a competitive mechanism among the grain refinement, strengthening effect, and texture weakening effect. Some new orientation fiber textures form with the increase in the Zn content from 0wt% to 1.0wt%, as shown in Fig. 10, and the intensity of the basal texture decreases from 6.27 to 4.36, as seen in Fig. 9. This condition results in a slight increase of UTS (229 MPa to 230 MPa) and a slight decrease of YS (171 MPa to 167 MPa), as shown in Fig. 11 for the 1.0Zn alloy, because the precipitation amount of ternary $Ca_2Mg_6Zn_3$ phase is lower and its strengthening effect is weak. For the addition of 2wt% Zn, the mechanical properties obtain a synergistic effect, contributing to both texture and second-phase strengthening. At 2.0wt% to 3.0wt% Zn content, the texture weakening shown in Fig. 9(d) offsets the strengthening effect so that the YS tends to decrease.

Generally, the texture modification in magnesium alloys is often ascribed to the solid solubility of the respective element and the particle-stimulated nucleation of recrystallization. Thus, the mechanism of texture modification can be described as follows: First, from the 0Zn alloy to the 1.0Zn alloy, the solid solution of Zn in Mg alloy may change the axial ratio (c/a) or stacking fault energy, thereby influencing the mechanical properties, dislocation cross slip, and dynamic recrystallization. This phenomenon results in the weakening and concentrating distribution along the TD of the textures, as shown in Fig. 9(b). Increased precipitation of $Ca_2Mg_6Zn_3$ phases in the 2.0Zn alloy blocks dislocation motion and refines the grains, thereby leading to stimulated nucleation of recrystallization during hot extrusion. Thus, the textures strengthen from 1.0Zn to 2.0Zn alloy, as shown in Fig. 9(c). However, further addition of Zn will induce a larger mean grain size and retard dynamic recrystallization, thereby decreasing the intensity of textures. Simply put, Zn can apparently affect the modification of textures by solid solution and nucleation of recrystallization.

Fig. 12(b) shows that the weight loss first decreases and then increases with Zn content from 0wt% to 3.0wt%. The minimum weight loss is obtained in the 1.0Zn alloy, which indicates that the 1.0Zn alloy has the best corrosion resistance among the four investigated alloys with different Zn contents. According to previous reports, the order of the standard electrode potentials of the phases in Mg–*x*Zn–0.2Ca alloys is $Mg_2Ca < Mg < Ca_2Mg_6Zn_3$. For the Mg–0.2Ca alloy, the Mg_2Ca phase acted as an anode and the Mg matrix acted as a cathode when the alloy samples are immersed in SBF [14]. Therefore, the pit can appear on the surface of alloy due to rapid dissolution of the Mg_2Ca phase anode, which can increase the contact area between the surface of alloy and the solution so that the process accelerates the corrosion reaction. From the 0Zn alloy to the 1.0Zn alloy, the second phase, the $Ca_2Mg_6Zn_3$ phase, is precipitated instead of Mg_2Ca. We can infer that the 1.0Zn alloy has a lower corrosion speed because the addition of Zn as a solution element in α-Mg matrix enhances the standard electrode potential of Mg and the second phase is also changed. The standard electrode potentials of $Ca_2Mg_6Zn_3$ is more positive than that of the α-Mg and Mg_2Ca phase; thus, the ternary $Ca_2Mg_6Zn_3$ phase is more difficult to degrade than the Mg_2Ca phase. However, from the 1.0Zn alloy to 3.0Zn alloys, the volume fractions of second phase $Ca_2Mg_6Zn_3$ and the grain boundaries increase gradually, which may lead to more galvanic corrosion reaction. In the 1.0Zn, 2.0Zn and 3.0Zn alloy, the $Ca_2Mg_6Zn_3$ phase acted as a cathode while the α-Mg matrix acted as an anode, thereby inducing the Mg matrix to corrode first, especially around the ternary $Ca_2Mg_6Zn_3$ phase. Gradually, the $Ca_2Mg_6Zn_3$ phase lost support from the Mg matrix and fell off naturally. As a result, corrosion holes and even cavities formed. Increased precipitation of the $Ca_2Mg_6Zn_3$ phase resulted in the formation of additional corrosion pits. The presence of corrosion pits accelerates the corrosion reactions, thereby explaining why the 2.0Zn and 3.0Zn alloys have a more undesirable corrosion resistance than the 1.0Zn alloy.

5. Conclusion

In the extruded Mg–*x*Zn–0.2Ca alloys, the grain size is refined with the increase in the Zn contents due to fully dynamic recrystallization. The addition of Zn element significantly influences the quantity of the second phase, the textures, the mechanical properties, and the corrosion properties in the Mg–*x*Zn–Ca alloys. The following conclusions were derived:

(1) The addition of Zn can lead to the formation of the ternary $Ca_2Mg_6Zn_3$ phase instead of Mg_2Ca. In addition, the precipitation amounts of the secondary phase increase with high Zn concentration.

(2) For the 2.0Zn alloy, the maximum UTS (278 MPa) and YS (230 MPa) are attained because of the more refined grain size and the strengthening effect of the second phase.

(3) The addition of Zn has a strong effect on altering the orientation and intensity of the textures, thereby influencing the mechanical properties.

(4) With the increase in Zn content, the corrosion rate first decreases and then increases from 1.0Zn alloy to 3.0Zn alloy. A minimum corrosion rate can be attained for the 1.0Zn alloy, which can be speculated as the difference of the quantity and electrochemical characteristics of diverse precipitated phases.

Acknowledgements

The Major State Research and Development Program of China (No. 2016YFB0300801), the National Natural Science Foundation of China (Nos. 51671017 and 51971020), the Fundamental Research Funds for the Central Universities (No. FRF-IC-19-010), Beijing Laboratory of Metallic Materials and Processing for Modern Transportation, the fund of the State Key Laboratory of Solidification Processing in NWPU (No. SKLSP201835), and the Opening Research Fund of State Key Laboratory for Advanced Metals and Materials (2018-Z04) are deeply appreciated for their financial support.

References

[1] H.R. Baksheesh-Rad, E. Hamzah, A. Fereidouni-Lotfabadi, M. Daroonparvar, M.A.M. Yajid, M. Mezbahul-Islam, M. Kasiri-Asgarani, and M. Medraj, Microstructure and bio-corrosion behavior of Mg–Zn and Mg–Zn–Ca alloys for biomedical applications, *Mater. Corros.*, 65(2014), No. 12, p. 1178.

[2] H.S. Brar, J.P. Ball, I.S. Berglund, J.B. Allen, and M.V. Manuel, A study of a biodegradable Mg–3Sc–3Y alloy and the effect of self-passivation on the in vitro degradation, *Acta Biomater.*, 9(2013), p. 5331.

[3] L.B. Tong, M.Y. Zheng, L.R. Cheng, S. Kamado, and H.J. Zhang, Effect of extruded ratio on microstructure, texture and mechanical properties of indirectly extruded Mg–Zn–Ca alloy, *Mater. Sci. Eng. A*, 569(2013), p. 48.

[4] Y.Z. Du, M.Y. Zheng, C. Xu, X.G. Qiao, K. Wu, X.D. Liu, G.J. Wang, and X.Y. Lv, Microstructures and mechanical properties of as-cast and as-extruded Mg–4.50Zn–1.13Ca (wt%) alloys, *Mater. Sci. Eng. A*, 576(2013), p. 6.

[5] M. Hradilová, D. Vojtěch, J. Kubásek, J. Čapek, and M. Vlach, Structural and mechanical characteristics of Mg–4Zn and Mg–4Zn–0.4Ca alloys after different thermal and mechanical processing routes, *Mater. Sci. Eng. A*, 586(2013), p. 284.

[6] H.R. Bakhsheshi-Rad, M.H. Idris, M.R. Abdul-Kadir, A. Ourdjini, M. Medraj, M. Daroonparvar, and E. Hamzah, Mechanical and bio-corrosion properties of quaternary Mg–Ca–Mn–Zn alloys compared with binary Mg–Ca alloys, *Mater. Des.*, 53(2014), p. 283.

[7] J. Yang, J. Peng, M. Li, E.A. Nyberg, and F.S. Pan, Effects of Ca addition on the mechanical properties and corrosion behavior of ZM21 wrought alloys, *Acta Metall. Sin. (Engl. Lett.)*, 30(2017), No. 1, p. 53.

[8] P. Yin, N.F. Li, T. Lei, L. Liu, and C. Ouyang, Effects of Ca on microstructure, mechanical and corrosion properties and biocompatibility of Mg–Zn–Ca alloys, *J. Mater. Sci. - Mater. Med.*, 24(2013), No. 6, p. 1365.

[9] B.P. Zhang, L. Geng, L.J. Huang, X.X. Zhang, and C.C. Dong, Enhanced mechanical properties in fine-grained Mg–1.0Zn–0.5Ca alloys prepared by extruded atdifferent temperatures, *Scr. Mater.*, 63(2010), No. 10, p. 1024.

[10] J. Hofstetter, S. Rüedi, I. Baumgartner, H. Kilian, B. Mingler, E. Povoden-Karadeniz, S. Pogatscher, P.J. Uggowitzer, and J.F. Löffler, Processing and microstructure–property relations of high-strength low-alloy (HSLA) Mg–Zn–Ca alloys, *Acta Mater.*, 98(2015), p. 423.

[11] L.B. Tong, M.Y. Zheng, X.S. Hu, K. Wu, S.W. Xu, S. Kamado, and Y. Kojima, Influence of ECAP routes on microstructure and mechanical properties of Mg–Zn–Ca alloy, *Mater. Sci. Eng. A*, 527(2010), No. 16-17, p. 4250.

[12] T. Kokubo and H. Takadama, How useful is SBF in predicting in vivo bone bioactivity, *Biomaterials*, 27(2006), No. 15, p. 2907.

[13] D. Zander and N.A. Zumdick, Influence of Ca and Zn on the microstructure and corrosion of biodegradable Mg–Ca–Zn alloys, *Corros. Sci.*, 93(2015), p. 222.

[14] E. Zhang and L. Yang, Microstructure, mechanical properties and bio-corrosion properties of Mg–Zn–Mn–Ca alloy for biomedical application, *Mater. Sci. Eng. A*, 497(2008), No. 1-2, p. 111.

[15] A. Takeuchi and A. Inoue, Classification of bulk metallic glasses by atomic size difference, heat of mixing and period of constituent elements and its application to characterization of the main alloying element, *Mater. Trans.*, 46(2005), No. 12, p. 2817.

[16] K. Kubok, L. Litynska-Dobrzynska, J. Wojewoda-Budka, A. Góral, and A. Debski, Investigation of structures in as-cast alloys from the Mg–Zn–Ca system, *Arch. Metall. Mater.*, 58(2013), No. 2, p. 399.

[17] G. Levi, S. Avraham, A. Ziberov, and M. Bamberger, Solidification, solution treatment and age hardening of a Mg–1.6wt% Ca–3.2wt% Zn alloy, *Acta Mater.* 54(2006), No. 2, p. 523.

[18] Y. Lu, A.R. Bradshaw, Y. L. Chiu, and I.P. Jones, Effects of secondary phase and grain size on the corrosion of biodegradable Mg–Zn–Ca alloys, *Mater. Sci. Eng. C*, 48(2015), p. 480.

[19] L. Geng, B.P. Zhang, A.B. Li, and C.C. Dong, Microstructure and mechanical properties of Mg–4.0Zn–0.5Ca alloy, *Mater. Lett.*, 63(2009), No. 5, p. 557.